

Theory of Ferroelectric ZrO₂ Monolayers on Si

Mehmet Dogan^{*,1,2,3,4} and Sohrab Ismail-Beigi^{1,2,5,6}

¹*Center for Research on Interface Structures and Phenomena,
Yale University, New Haven, Connecticut 06520, USA*

²*Department of Physics, Yale University,
New Haven, Connecticut 06520, USA*

³*Department of Physics, University of California,
Berkeley, California 94720, USA*

⁴*Materials Science Division,
Lawrence Berkeley National Laboratory,
Berkeley, California 94720, USA*

⁵*Department of Applied Physics, Yale University,
New Haven, Connecticut 06520, USA*

⁶*Department of Mechanical Engineering and Materials Science,
Yale University, New Haven, Connecticut 06520, USA*

**Corresponding author: mhmtdogan@gmail.com*

(Dated: January 31, 2019)

We use density functional theory and Monte Carlo lattice simulations to investigate the structure of ZrO₂ monolayers on Si(001). Recently, we have reported on the experimental growth of amorphous ZrO₂ monolayers on silicon and their ferroelectric properties, marking the achievement of the thinnest possible ferroelectric oxide [M. Dogan et al. *Nano Lett.*, **18** (1) (2018) [1]]. Here, we first describe the rich landscape of atomic configurations of monocrystalline ZrO₂ monolayers on Si and determine the local energy minima. Because of the multitude of low-energy configurations we find, we consider the coexistence of finite-sized regions of different configurations. We create a simple nearest-neighbor lattice model with parameters extracted from DFT calculations, and solve it numerically using a cluster Monte Carlo algorithm. Our results suggest that up to room temperature, the ZrO₂ monolayer consists of small domains of two low-energy configurations with opposite ferroelectric polarization. This explains the observed ferroelectric behavior in the experimental films as a collection of crystalline regions, which are a few nanometers in size, being switched with the application of an external electric field.

I. INTRODUCTION

Thin films of metal oxides have been a focus area of continuous research due to the rich physics that can be observed in these systems, such as ferroelectricity, ferromagnetism and superconductivity, and their resulting technological applications [2, 3]. An important challenge involving thin metal oxide films has been their growth on semiconductors in such a way that their electrical polarization couples to the electronic states inside the semiconductor [4–6]. If successfully done, this enables the development of non-volatile devices such as ferroelectric field-effect transistors (FEFET). In a FEFET, the polarization of the oxide encodes the state of the device, and requires the application of a gate voltage only for switching the state, greatly reducing the power consumption and boosting the speed of the device [7, 8]. Meeting this challenge requires a thin film ferroelectric oxide, as well as an atomically abrupt interface between the oxide and the semiconductor, so that the polarization of the oxide and the electronic states in the semiconductor are coupled. The first of these requirements, i.e., a thin film ferroelectric, is difficult to obtain because materials that are ferroelectric in the bulk lose their macroscopic polarization below a critical thickness, due to the depolarizing field created by surface bound charges [9, 10]. An al-

ternative approach is to search for materials such that, regardless of their bulk properties, they are stable in multiple polarization configurations as thin films [6]. The second requirement, i.e., an abrupt oxide-semiconductor interface, has been challenging due to the formation of amorphous oxides such as SiO₂ at the interface with a semiconductor such as Si [8, 11, 12]. This challenge has been overcome by using layer-by-layer growth methods such as molecular beam epitaxy (MBE) and employing highly controlled growth conditions [7, 13, 14].

We recently reported on the experimental observation of polarization switching in atomically thin ZrO₂ grown on Si [1]. In the experimental setup, ZrO₂ was grown using atomic layer deposition (ALD), yielding an amorphous oxide and an abrupt oxide-silicon interface with no significant formation of SiO₂. This interface was then incorporated into a gate stack device with amorphous Al₂O₃ separating it from the top electrode. Ferroelectric behavior was observed by $C - V$ measurements with this gate stack. In this work, we present an in-depth computational investigation of this monolayer system.

In Section §II, we describe our computational methods. In section III A, we investigate the structure of free-standing ZrO₂ monolayers assuming they are strained to the two-dimensional lattice of the Si(001) surface. In section III B, we report on the low-energy configurations

of these monolayers when placed on the Si(001) surface. We find that these films have multiple (meta)stable structures with no significant chemical monocrystalline growth between them. This suggests that epitaxial monocrystalline growth may be challenging. In section III C, we examine the domain energetics in this system: we build a lattice model with nearest-neighbor interactions, and solve this model using a Monte Carlo cluster method. The results of the lattice model provide a microscopic understanding of the experimentally observed polarization switching.

II. COMPUTATIONAL METHODS

We theoretically model the materials systems using density functional theory (DFT) with the Perdew–Burke–Ernzerhof generalized gradient approximation (PBE GGA) [15] and ultrasoft pseudopotentials [16]. We use the QUANTUM ESPRESSO software package [17]. A 35 Ry plane wave energy cutoff is used to describe the pseudo Kohn–Sham wavefunctions. We sample the Brillouin zone with an $8 \times 8 \times 1$ Monkhorst–Pack k -point mesh (per 1×1 in-plane primitive cell) and a 0.02 Ry Marzari–Vanderbilt smearing [18]. A typical simulation cell consists of 8 atomic layers of Si whose bottom layer is passivated with H and a monolayer of ZrO_2 placed on top (see Figure 1). Periodic copies of the slab are separated by $\sim 12\text{\AA}$ of vacuum in the z -direction. The in-plane lattice constant is fixed to the computed bulk Si lattice constant of 3.87\AA . In general, the slab has an overall electrical dipole moment along the z direction that might artificially interact with its periodic images across the vacuum. In order to prevent this unphysical effect, we introduce a fictitious dipole in the vacuum region of the cell which cancels out the electric field in vacuum and removes such interactions [19]. All atomic coordinates are relaxed until the forces on all the atoms are less than $10^{-3}\text{Ryd}/a_0$ in all axial directions, where a_0 is the Bohr radius (except the bottom 4 layers of Si which are fixed to their bulk positions to simulate a thick Si substrate). We use the nudged elastic bands (NEB) method with climbing images [20] to compute the transition energy barrier between different metastable configurations.

III. RESULTS

A. Free standing ZrO_2 monolayers

1. Background: bulk zirconia

Bulk ZrO_2 is observed in three structural phases. The high symmetry cubic phase (space group: $Fm\bar{3}m$) is shown in Figure 2. The lower symmetry tetragonal ($P4_2/nmc$) and monoclinic ($P2_1/c$) phases are obtained by continuously breaking the symmetries of the cubic

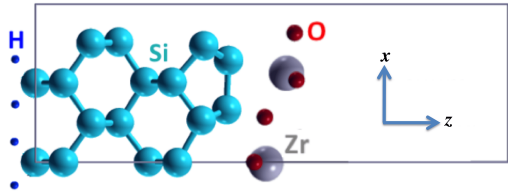


Figure 1. A typical simulation supercell with 2×1 in-plane periodicity. The bottom 4 layers of Si are fixed to bulk coordinates and passivated by hydrogen as shown, to simulate bulk silicon. There is $\sim 12\text{\AA}$ of vacuum along the z -direction to separate periodic copies.

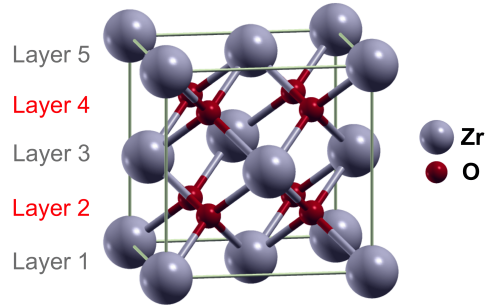


Figure 2. The high symmetry cubic phase ($Fm\bar{3}m$) of bulk ZrO_2 . Atomic layers are labelled 1 through 5, where the odd (even) layers correspond to cation (anion) planes.

phase. All three configurations are centrosymmetric and hence not ferroelectric. However, this binary oxide has a *layered structure* (along low-index directions) in which the cations and anions lie in different planes, which, in thin film stoichiometric form, would cause ultrathin ZrO_2 films to be polar. For instance, in Figure 2 a horizontal monolayer of ZrO_2 could be formed by the zirconium atoms in Layer 3, with (a) the oxygen atoms in Layer 2, or with (b) the oxygen atoms in Layer 4, or with (c) half of the oxygen atoms in each of Layer 2 and Layer 4. Before relaxing the atoms in these hypothetical monolayers, in case (a) the resulting polarization would be upward, in case (b) it would be downward, and in case (c) it would be zero. This intrinsic layered structure, which is also preserved in the tetragonal and the monoclinic phases of zirconia, is a fundamental reason why ZrO_2 is an excellent candidate to have a switchable polarization when grown on silicon.

2. Structure of free standing monolayers

In order to check if this richness of structure due to the layered nature of the bulk material is retained in

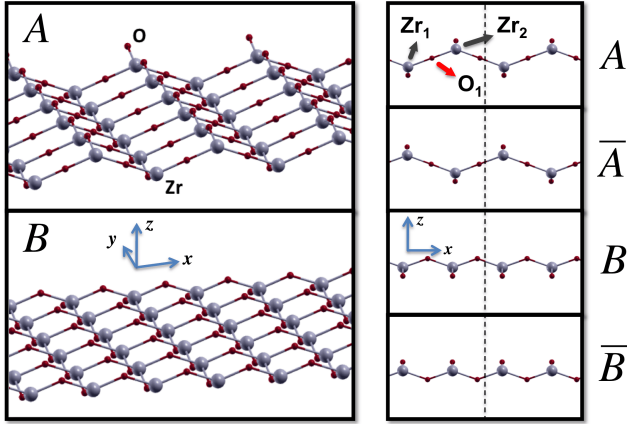


Figure 3. The lowest energy configurations of the free standing ZrO_2 monolayer. Structure B has an energy of 0.07 eV per ZrO_2 above that of structure A . On the right, all four geometrically distinct metastable configurations are shown. \bar{A} and \bar{B} are obtained from A and B , respectively, by reflection in the $z = 0$ plane. For each structure, two copies of the 2×1 unit cells are displayed and a vertical dashed line separates the copies.

the ultrathin film, we have simulated free standing ZrO_2 monolayers. A monolayer formed by a (001) plane of cubic ZrO_2 would have a square lattice with size 3.61 Å (based on our DFT computations). To match the lattice of the Si substrate, we simulate the monolayers at the lattice constant of the Si(001) surface, which we find to be 3.87 Å. We have searched for minimum energy configurations for 1×1 , 2×1 , 2×2 and $c(4 \times 2)$ sized unit cells of monolayer ZrO_2 which are the periodicities of the low energy reconstructions of the bare Si(001) surface, as we shall discuss in section III B.

We find that the lowest and the second lowest energy configurations of the ZrO_2 monolayer are 2×1 and 1×1 , respectively, as shown in Figure 3. The chief difference between the two configurations is that the lowest energy structure, labeled A , has a vertical (along z) buckling of zirconiums in the $2 \times$ in-plane direction, while for the second lowest energy structure, labeled B , all the Zr are coplanar. We find that $E(B) - E(A) = 0.07$ eV per ZrO_2 . Both of these configurations are inversion symmetric and hence non-polar. However, because neither A or B is symmetric with respect to the mirror plane reflection $z \rightarrow -z$, there are two more geometrically distinct minima, named \bar{A} and \bar{B} , which are shown in Figure 3. \bar{A} and \bar{B} are obtained from A and B , respectively, by the mirror reflection. Notice that \bar{A} can be obtained from A also by translating in the $2 \times$ direction by half a 2×1 cell. However, since the underlying substrate will have at least 2×1 periodicity, this translation would not leave the entire system (ZrO_2 with substrate) invariant.

3. Energy landscape of free standing monolayers

In order to analyze these configurations further, we parametrize the energy landscape of free standing ZrO_2 monolayers by using two coordinates: $z_1 \equiv z(\text{Zr}_2) - z(\text{Zr}_1)$ and $z_2 \equiv z(\text{O}_1) - z(\text{Zr}_1)$, where the atoms Zr_1 , Zr_2 and O_1 are labeled for structure A in Figure 3 (for structures \bar{A} , B and \bar{B} , Zr_1 is directly below Zr_1 of structure A in the figure, and similarly for Zr_2 and O_1). Note that the structures B and \bar{B} are treated in 2×1 unit cells for this analysis. To explore the energy landscape, we have made a 9×9 grid of (z_1, z_2) values and computed corresponding energies for structures whose z_1 and z_2 are fixed but all other coordinates are relaxed. In Figure 4, we plot the energy landscape using darker (lighter) colors to represent lower (higher) energies. The coloring is implemented by MatLab's linear interpolation scheme based on the DFT energies on an equally spaced 9×9 grid. We also label the four (meta)stable configurations on the landscape. The energies are reported for 2×1 cells where $E(A) = E(\bar{A}) = 0$ is set as the zero of energy.

In Figure 4 we also present the minimum energy transition paths between these energy minima, as thick solid curves. We have found these transitions using the NEB method with climbing images [20]. There are 6 pairs of metastable configurations and hence 6 transition paths: $A \leftrightarrow \bar{A}$, $A \leftrightarrow B$, $A \leftrightarrow \bar{B}$, $\bar{A} \leftrightarrow B$, $\bar{A} \leftrightarrow \bar{B}$ and $B \leftrightarrow \bar{B}$. However, as seen from the figure, the transition paths of $A \leftrightarrow \bar{A}$ and $B \leftrightarrow \bar{B}$ go through other energy minima and hence can be expressed in terms of the remaining 4 transitions. We have found that all of the four transitions go through a transition state with energy 1.04 eV per 2×1 cell. These four saddle points, shown as diamond marks in Figure 4, are related by reflection and/or translation operations, and hence are physically equivalent.

To sum up, we have found that as a free standing monolayer in vacuum, ZrO_2 is not polar but has two physically distinct stable configurations. In the presence of a surface that breaks the $z \rightarrow -z$ symmetry, A and \bar{A} (as well as B and \bar{B}) have the potential to relax to new configurations that are differently polarized.

B. ZrO_2 monolayers on Si(001)

1. Bare Si(001) surface

To study the behavior of zirconia on Si(001), we first review the structure of the bare Si(001) surface. It is well known that, on the Si(001) surface, neighboring Si atoms pair up to form dimers [21, 22], and we find that dimerization lowers the energy by 1.45 eV per dimer. The dimers can buckle (i.e., the two Si forming the dimer do not have the same out-of-plane z coordinate) which lowers their energy. If nearby dimers buckle in opposite ways, higher order reconstructions occur. We summarize

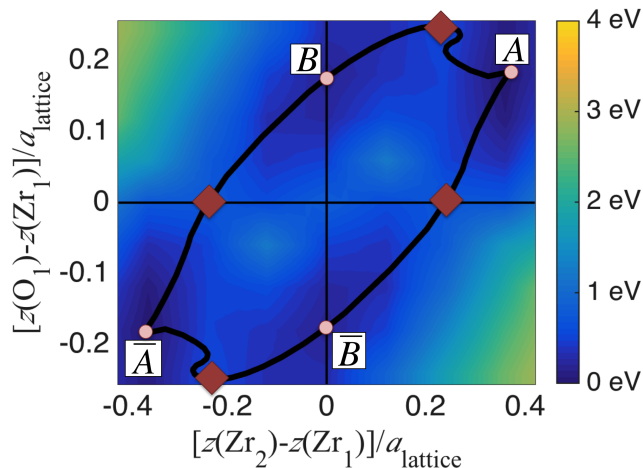


Figure 4. The energy landscape of the free standing ZrO_2 monolayer, as parametrized by a pair of coordinates $z_1 \equiv z(\text{Zr}_2) - z(\text{Zr}_1)$ and $z_2 \equiv z(\text{O}_1) - z(\text{Zr}_1)$ (See Figure 3 for labelings of the atoms). a_{lattice} is the computed lattice constant of silicon and is equal to 3.87 Å. All four local energy minima as well as the minimum energy transition paths between them are shown. The saddle points on the landscape (i.e., the transition states) are shown as diamonds. The zero of energy is taken to be the energy of structure A. All transition states lie at the same energy because they are related by reflection/translation operations. The energy landscape is computed by DFT on a 9×9 grid and then interpolated by MatLab to produce the smooth colored plot.

Si surface	Energy (eV/dimer)	Ref. [21]	Ref. [22]
flat $p(2 \times 1)$	$\equiv 0.00$	$\equiv 0.00$	$\equiv 0.00$
buckled $p(2 \times 1)$	-0.20	-0.12	-0.13
buckled $p(2 \times 2)$	-0.28	-0.17	-0.23
buckled $c(4 \times 2)$	-0.27	-0.17	-0.24

Table I. Energies of the lowest energy Si(001) surface reconstructions per dimer. Two theoretical references are presented alongside our computed results. See the cited works for details of the listed reconstructions.

the energies of these reconstructions in Table I (we refer the reader to the cited works for detailed descriptions of these surface configurations). There is a strong drive for the surface Si atoms to dimerize (transition from a 1×1 to a 2×1 unit cell) and a weaker energetic drive to organize the dimers into structures with periodicities larger than 2×1 . Because the metastable configurations of the ZrO_2 monolayers we found above have unit cells that are 2×1 or smaller, we have limited our search for Si/ ZrO_2 interfaces to 2×1 simulation cells.

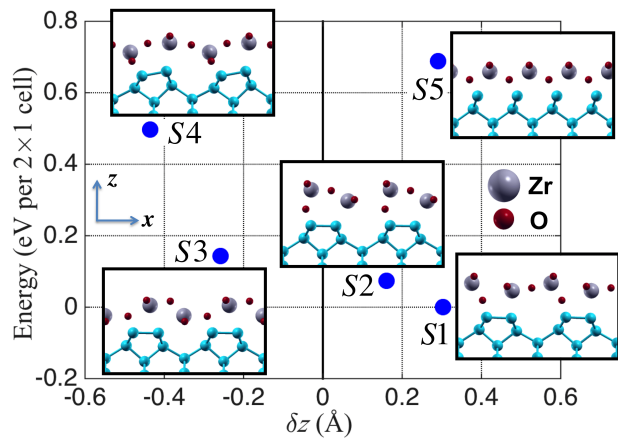


Figure 5. Five lowest energy configurations of ZrO_2 monolayers on Si. $\delta z \equiv z(\text{Zr}) - z(\text{O})$ is a measure of ionic out-of-plane polarization for the monolayers. Energies are listed in eV per 2×1 in-plane cell measured with respect to the lowest energy structure S1.

2. Structure of the monolayers on silicon

We have searched the configuration space for ZrO_2 on Si(001) as follows: First, we have created a $3 \times 3 \times 2$ grid of points inside the 2×1 in-plane unit cell on top of the bare Si surface where a Zr atom is placed (the 3×3 grid corresponds to points in the xy -plane and the $\times 2$ corresponds to the vertical distance from the substrate). A flat and high symmetry 1×1 zirconia monolayer is generated such that it includes this Zr atom. For each such structure, the atoms in the Si surface layer and the ZrO_2 monolayer are randomly and slightly displaced to generate 5 initial positions. This procedure, which yields $3 \times 3 \times 2 \times 5 = 90$ configurations, is done for dimerized and non-dimerized Si surfaces, so that there are 180 initial configurations in total. We have then relaxed all the atoms in ZrO_2 and the top 4 layers of silicon substrate to find local energy minima.

We present the five lowest energy structures we have obtained in Figure 5. The horizontal axis is a quantity that describes the ionic polarization of the ZrO_2 monolayer and is defined as the mean vertical Zr-O separation $\delta z \equiv \overline{z(\text{Zr})} - \overline{z(\text{O})}$, where over-bars mean averaging of the coordinate over the atoms of that type in the structure. The vertical axis is the energy in eV per 2×1 cell measured with respect to the lowest energy structure, labeled S1. The energies of S1 through S5 are also listed in Table II.

First, the metastable configurations lie on both sides of the $\delta z = 0$ line, which means that there is no polarization direction that is strongly preferred. Second, we find that the four lowest energy structures have a 2×1 periodicity with intact Si dimers. (In addition to S5,

	$S1$	$S2$	$S3$	$S4$	$S5$
Energy (eV per 2×1 cell)	$\equiv 0.00$	0.07	0.14	0.50	0.69

Table II. Energies of the five lowest energy configurations of ZrO_2 monolayers on Si as labeled in Figure 5.

we have found three more 1×1 structures with broken dimers at energies higher than 1 eV that are not shown.) The energy difference of 0.69 eV per dimer between the lowest energy 1×1 and the lowest energy 2×1 structures (i.e. $S5$ and $S1$) is half of the energy of dimerization on the bare Si surface. Moreover, the length of the dimer in $S1$ is 2.42 Å which is longer than the 2.31 Å on the bare surface. Therefore, in general, the Si dimers are weakened but not broken by the ZrO_2 monolayer for the more stable low-energy structures.

Third, we notice that for each configuration shown in Figure 5, a physically equivalent configuration is obtained by a mirror reflection by the yz -plane, which doubles the number of metastable structures in the configuration space. For our analysis of transitions between these configurations, we make the reasonable assumption that silicon dimers remain intact during the transition between two dimerized configurations. Hence, we reflect the atomic positions through a yz -plane which keeps the dimers in place in order to obtain the geometrically inequivalent (but physically identical) set of structures $\overline{S1}$, $\overline{S2}$ etc.

3. Transitions between low energy states

We have computed the minimum energy transition paths between the three lowest energy configurations and their symmetry related counterparts ($S1, \overline{S1}, S2, \overline{S2}, S3, \overline{S3}$). When applying the NEB method to find transition states, each atom in the initial configuration is mapped to an atom in the final configuration. In principle, all possible matching choices should be attempted in order to find all inequivalent transition paths and energy barriers. However, this is neither practical nor physically necessary. For the case of free standing ZrO_2 , in all the minimum energy configurations, all atomic (x, y) coordinates line on a square grid, and by making the reasonable assumption that atoms do not swap sites during the transition, we can dramatically reduce the number of possible transition paths under consideration. Hence, we matched each atom in the initial configuration with the atom that sits at the same (x, y) site in the final configuration in order to perform the NEB calculations. Even though no fixed square grid exists for

the ZrO_2/Si case that applies to all the configurations, similar considerations are possible: (1) For the six configurations of interest, both Zr atoms and two out of the four O atoms in a unit cell align along the y -direction with the Si dimers ($y = 0.5a_{\text{lat}}$), and the other two O atoms lie half way between consecutive dimers ($y = 0$). Both along the x - and the y -directions, atomic chains of $\dots\text{-Zr-O-Zr-O-}\dots$ exist in all cases. So for each configuration, we can make a square grid in the xy -plane such that one Zr per cell sits at a lattice site and the other atoms are very close to the other lattice sites. For each transition process, the grid is assumed only to shift in the x -direction. (2) Because of the high energy cost of breaking Si dimers on the bare Si(001) surface, we assume that the dimers remain intact during a transition. (3) We assume that $\dots\text{-Zr-O-Zr-O-}\dots$ chains along the y -direction remain intact during a transition, so no movement in the y -direction is considered.

By using these constraints, we can reduce the number of possible matchings to four for each transition. We demonstrate these choices for the transition $S1 \rightarrow S2$ in Figure 6. The final state $S2$ is displayed upside down in order allow for a clearer illustration of atomic matchings. In the left panel, $\dots\text{-Zr-O-Zr-O-}\dots$ chains along the y -direction are circled by blue dashed rings. There are two possible ways in which the chains in $S1$ can be matched to the chains in $S2$ that do not cause large scale rearrangements. One of these matchings is shown as solid arrows, and the other is shown as dotted arrows. In the right panel, the same exercise is repeated for the remaining oxygens (circled by red dashed rings). Therefore there are $2 \times 2 = 4$ matchings in total. Note that the reverse processes correspond to the set of matchings that obey our rules for the transition $S2 \rightarrow S1$.

The resulting smallest energy barriers are listed in Table III. Notice that the nine listed transitions cover all the possible transitions because, e.g., the transition $S1 \leftrightarrow S2$ is related by symmetry to $\overline{S1} \leftrightarrow \overline{S2}$. We observe that the transitions within the set of unbarred states are about 1 eV smaller than the transitions between unbarred and barred states. This is understood as follows: for all six structures, there is one oxygen per cell which binds to a silicon atom. The transitions that leave that oxygen in place (such as the dotted arrows in the right panels of Figure 6) have lower energy barriers. A transition between an unbarred state and a barred state necessarily involves displacing that oxygen and breaking the strong Si-O bond. Therefore a low energy path is not possible in such a case.

Focusing on the three low energy transitions, i.e. $S1 \leftrightarrow S2$, $S1 \leftrightarrow S3$ and $S2 \leftrightarrow S3$, we plot energy vs δz curves in Figure 7. The transition state of $S2 \leftrightarrow S3$ (dotted curve) and the shared transition state of $S1 \leftrightarrow S2$ and $S1 \leftrightarrow S3$ (solid curves) are marked by diamonds on the plot and their configurations are displayed. During these transitions, the oxygen atom that is bonded to a sili-

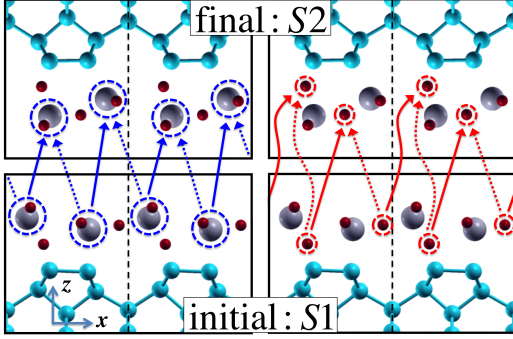


Figure 6. The possible matchings for the $S1 \rightarrow S2$ transition for the NEB simulation. The $S2$ structure is displayed upside down to allow for ease of understanding the matching. In the left panels, two possible choices for the two Zr-O pairs (or chains) in the $S1$ unit cell that are to be matched to the Zr-O pairs (or chains) in the structure $S2$ are shown. The set of solid arrows corresponds to one choice, and the set of dotted lines corresponds to another choice. Similarly, two choices for the remaining oxygens are displayed in the right panels. See text for further details of the described matchings. Two periodic copies of 2×1 cells are shown in each case, and a dashed line is drawn to separate the copies.

Transition	$E_{\text{barrier}} (\rightarrow)$ (eV)	$E_{\text{barrier}} (\leftarrow)$ (eV)
$S1 \leftrightarrow \overline{S1}$	1.63	1.63
$S1 \leftrightarrow S2$	0.79	0.71
$S1 \leftrightarrow \overline{S2}$	1.60	1.52
$S1 \leftrightarrow S3$	0.79	0.65
$S1 \leftrightarrow \overline{S3}$	1.60	1.46
$S2 \leftrightarrow \overline{S2}$	2.48	2.48
$S2 \leftrightarrow S3$	0.23	0.17
$S2 \leftrightarrow \overline{S3}$	1.57	1.51
$S3 \leftrightarrow \overline{S3}$	1.77	1.77

Table III. Transition barriers, calculated via the NEB method, between pairs of low energy configurations of ZrO_2 monolayers on $\text{Si}(001)$. Energy barriers are reported in eV per 2×1 cell. The central and rightmost columns show the barriers going in both directions (as indicated by the arrow directions).

con (circled by red dashed rings in the figure) remains in place, while the remaining 5 atoms in the ZrO_2 layer (inside the blue dashed rounded rectangles) move in concert. Because this movement does not significantly alter the chemistry of the interface, the energy barriers are relatively low.

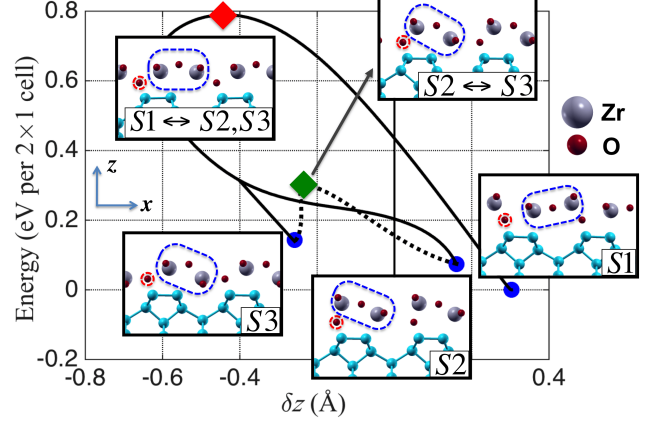


Figure 7. Three lowest energy configurations of ZrO_2 monolayers on Si and the transition paths between them calculated via the NEB method. The solid curve corresponds to the transitions $S1 \leftrightarrow (S2, S3)$ that share a transition state denoted by a red diamond. The dotted curve corresponds to the transition $S2 \leftrightarrow S3$ which has a transition state denoted by a green diamond. The circled oxygen atoms remain in place during the transitions, and the circled groups of five atoms move as a block with small internal displacements.

Because of the rich landscape of stable configurations at low energy with similar chemical bonding and small structural differences, we predict that growing large single-crystalline epitaxial films of ZrO_2 on $\text{Si}(001)$ should be challenging. However, epitaxy may not be a necessary condition for ferroelectricity in this system. A close examination of the structures shown in Figure 7 indicates that the symmetry of the silicon surface, as well as the inherently rumpled structure of ZrO_2 , give rise to the switchable polarization. The switching of the dipole occurs by a continuous displacement of a group of atoms in the unit cell, while one oxygen remains in place. No significant chemical change occurs during these transitions. We note that open channels in the dimerized (001) face of silicon allow for the motion of the oxide atoms lacking silicon nearest neighbors, which stabilizes the three low-energy polar ZrO_2 structures.

4. Coupling of polarization to electronic states in Si

In addition to the prediction that the three lowest energy structures may coexist in monolayer form, in section III C we will explain why, at temperatures of practical interest, structures $S2$ and $S3$ should be the dominant motifs in the monolayer structure. Because of the large difference in polarization together with a low energy barrier between these two structures, we believe that the polarization switching described in Ref. [1] should cor-

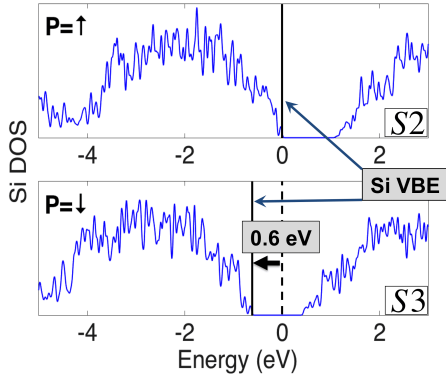


Figure 8. Density of states in an interior Si layer with the ZrO_2 film in its upwardly polarized ($S2$) and downwardly polarized ($S3$) forms. There exists a valence band edge (VBE) shift between the "up" state (top) and the "down" state (bottom). This figure is reproduced from Ref. [1].

respond to switching between $S2$ and $S3$. A first and simple corroboration involves showing that the change in the silicon Fermi level observed in the experiment is comparable with our theoretical prediction. In Figure 8, we plot the density of states (DOS) of the ZrO_2/Si system projected onto an interior layer of the Si substrate for the cases of interface structures $S2$ and $S3$. We set the energy of the Si valence band edge (VBE) of $S2$ to zero and align the vacuum energy level in $S3$ to the vacuum energy level in $S2$. We find a 0.6 eV VBE shift in Si, which is somewhat larger than, but comparable to, the experimental value of 0.4 eV. We believe that this is due to the fact that the experimental monolayers are not epitaxial but amorphous with multiple structural motifs present, so that application of the electric field is not as effective at polarization switching as is assumed in our clean, epitaxial and ordered theoretical simulations.

C. Domain energetics

Up to this point, our theoretical study of the ZrO_2 monolayers on the $\text{Si}(001)$ surface has shown that (meta)stable configurations with varying polarizations are present. We have also demonstrated that transitions between some of the lowest energy configurations do not require complicated rearrangements of atoms and have low energy barriers. Because of these findings, as well as the fact that the experimental monolayer is amorphous, we expect there to be a multi-domain character to these monolayers at or near room temperature ($k_B T = 0.026$). However, directly calculating the energy of a multi-domain region of the system for an area

larger than a few primitive unit cells is not feasible. In this section, we describe an approximate model Hamiltonian method to compute the energies of arbitrary regions of multiple domains, and use Monte Carlo simulations to find thermodynamic ground states at finite temperatures.

1. Domain wall energies

In order to investigate the behavior of finite domains, we have developed a lattice model where every 2×1 in-plane cell is treated as a site in a two dimensional lattice which couples to its neighbors via an interaction energy. Similar models have been proposed for other two dimensional systems [23]. Such a model is reasonable if the interface (domain wall) between domains of different states is sharp, i.e., the atomic positions a few unit cells away from a domain boundary are indistinguishable from the atomic positions in the center of the domain. To find the degree of locality and the energy costs of the domain walls, we have computed domain wall energies as a function of domain size.

Sample simulation arrangements are shown in Figure 9. In (a) and (b), domain walls along the y - and x -directions are formed, respectively, between the configurations $S1$ and $S2$. Three unit cells of $S1$ and $S2$ each are generated and attached together to build larger simulation cells to model the domain walls: 12×1 and 2×6 cells to simulate the domain boundaries along the y - and x -directions, respectively. In each of the 3 unit wide domains, the center unit is fixed to the atomic configuration of the corresponding uniform system. In Figure 9, for the $S1$ domain, the atoms in the unit labelled $S1$ are fixed, and the atoms in the units $S1l$ and $S1r$ are relaxed. The same is true for $S2$, but for clarity, fixed units of $S2$ are displayed on both sides. We then compute the domain wall energy between $S1$ and $S2$ by subtracting $3E(S1) + 3E(S2)$ from the total energy of this supercell and dividing by two. We have checked for a few test cases that increasing the domain width from 3 to 5 cells changes the domain wall energies by small amounts on the order of 1-10 meV while typical domain wall energies are larger than 100 meV (see Table IV). This, together with visualization of the resulting structures, convinces us that the domains are sufficiently local for us to treat the domain walls as being sharp. Note that there are two inequivalent boundaries between $S1$ and $S2$ along a given direction. In Figure 9, these boundaries are shown as red and blue dashed lines. Due to the periodicity of simulation cells, it is not possible to compute the energies of these two boundaries independently, so we are forced to assume that their energies are equal.

The final step in determining the domain boundary energies is to survey the configuration space available for a given boundary. For that purpose, for each domain boundary we have generated a number of initial configura-

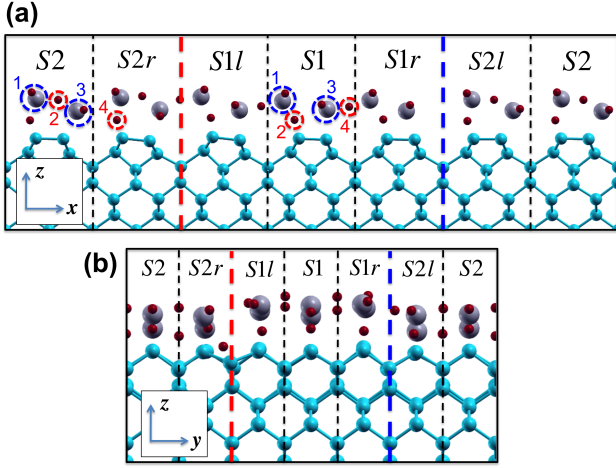


Figure 9. Simulation arrangements to compute the domain boundary energies between $S1$ and $S2$. (a) 3 cells each of $S1$ and $S2$ are stacked along the x -direction to form straight domain boundaries in the y -direction. The numberings of atomic groups within the unit cells are displayed using dashed circles. The boundary on the right (blue) is initially built by the atomic groups 1, 2 and 3 from $S1$ and 4 from $S2$ in the unit cell to the left of the boundary (labelled $S1r$), and the atomic groups 1, 2, 3 and 4 from $S2$ in the unit cell to the right of the boundary (labelled $S2l$). The boundary on the left (red) is constructed to preserve the number of atomic groups from each cell. (b) 3 cells each of $S1$ and $S2$ are stacked along the y -direction to form straight domain boundaries in the x -direction. Fully relaxed boundary configurations are shown.

rations depending on the direction of the boundary:

- For a boundary along the y -direction such as in Figure 9(a), we have generated five initial configurations as follows. For each domain state (e.g., $S1$ or $S2$), we have labeled the Zr-O pairs along the y -direction and the remaining oxygens and numbered them in an increasing order in the x -direction. In the figure, the labelling for states $S1$ and $S2$ is shown. Note that for each cell, the sequence starts with a Zr-O pair and ends with an O atom. Hence in some cases the oxygen labelled 4 lies beyond the unit cell to which it belongs, such as in $S2$. To build a domain boundary such as the $S1r$ - $S2l$ (shown as a blue dashed line), we first place the atomic groups numbered 1 – 4 from $S1$ to the left hand side of the boundary, and the atomic groups numbered 1 – 4 from $S2$ to the right hand side of the boundary. This constitutes our first initial configuration. The second configuration is obtained by replacing atom 4 from $S1$ on the left hand side by atom 4 from $S2$. The third is obtained by replacing both group 3 and atom 4 from $S1$ by 3 and 4 from $S2$. The fourth choice is to replace atomic group 1 from $S2$ on the right hand side by group 1 from $S1$; and, lastly, the

fifth choice is to replace 1 and 2 from $S2$ by 1 and 2 from $S1$. The opposite operation is performed at the other boundary such as $S2r$ - $S1l$ (shown as a red dashed line). We then take the smallest of the five computed domain energies as the final energy. Note that the relaxed structure shown in the Figure 9(a) for the $S1$ - $S2$ domain boundaries is obtained via choice #2 for the $S1r$ - $S2l$ boundary.

- For a boundary along the x -direction such as in Figure 9(b), we have generated a few initial configurations by slightly and randomly displacing the two oxygen atoms at the boundary along the y -direction in order to break the $y \rightarrow -y$ symmetry inherent to these structures.

2. Construction of a lattice model

Once we have the library of domain boundary energies for every pair of states along the x - and y -directions described above, we approximate the energy of the system with an arbitrary configuration of domains by a two-dimensional anisotropic lattice Hamiltonian on a square lattice:

$$H = \sum_{i,j} E(\sigma(i,j)) + \sum_{i,j} J_x(\sigma(i,j), \sigma(i+1,j)) + \sum_{i,j} J_y(\sigma(i,j), \sigma(i,j+1)), \quad (1)$$

where $\sigma(i)$ donates the state at a given site i , $E(\sigma(i))$ is the energy (per 2×1 unit cell) of state $\sigma(i)$ for a uniform system in that state, and $J_\alpha(\sigma(i), \sigma(j))$ is the energy of interaction (i.e., domain wall energy) between the neighboring states i, j in the axial direction α . In our model, only nearest neighbor interactions are included. Because of the anisotropic nature of the film (the x - and y -directions are fundamentally different due to Si dimerization), the interaction term must distinguish between directions x and y so that J_x and J_y differ. The domain boundary energies calculated via DFT simulations are employed as nearest neighbor interaction energies in this model. In Figure 10, we illustrate an arbitrary configuration of such a lattice. As an example, the state $S1$ in the middle column couples to $\overline{S1}$ and $S3$ via $J_x(S1, \overline{S1})$ and $J_x(S1, S3)$, respectively, and to $S2$ and $\overline{S2}$ via $J_y(S1, S2)$ and $J_y(S1, \overline{S2})$, respectively.

For a model with N distinct states, our interaction matrices J_α ($\alpha = x, y$) have the following properties:

- The interaction energy between the sites of the same kind is zero by definition, $J_\alpha(\sigma_i, \sigma_i) = 0$. Hence the number of non-zero entries is $N^2 - N$.
- We have assumed that the domain wall energy between states σ_i and σ_j remains the same if we swap

$S3$	$\overline{S2}$	$S2$	$\overline{S2}$	$S1$
$\overline{S1}$	$\overline{S1}$	$S1$	$S3$	$\overline{S1}$
$S1$	$S2$	$\overline{S2}$	$\overline{S3}$	$S2$
$\overline{S3}$	$S2$	$\overline{S3}$	$S3$	$\overline{S1}$

Figure 10. An example configuration of the two dimensional lattice that approximates the ZrO_2 monolayer on Si as a multi-domain system. Nearest neighbor sites couple through the coefficients J_x (blue arrows) and J_y (green arrows).

the states. Therefore the interaction matrices are symmetric $J_\alpha(\sigma_i, \sigma_j) = J_\alpha(\sigma_j, \sigma_i)$, reducing the number of unique non-zero entries to $\frac{1}{2}(N^2 - N)$.

- In our particular system, every state has a counterpart which is obtained by the reflection $x \rightarrow -x$. Hence, e.g., the domain wall between $\overline{S1}$ and $\overline{S2}$ can be obtained from the domain wall between $S1$ and $S2$ by applying a single symmetry operation. Therefore many of the entries of $J_\alpha(\sigma_i, \sigma_j)$ are paired up in this way which further reduces the number of unique entries further to $\frac{1}{4}N^2$.

In Table IV, we list the unique entries of $J_\alpha(\sigma_i, \sigma_j)$ for states σ ranging over the the six lowest energy states. Note that since $N = 6$ for this table, there are $\frac{1}{4}6^2 = 9$ entries in the table. Because the unit cell is 2×1 , the couplings J_x are expected to be smaller than the couplings J_y , which is generally correct. We have computed the domain wall energies for more possible of states including $S4$, $\overline{S4}$, $S5$ and $\overline{S5}$, and the longer list of resulting domain wall energies (see Supplementary Material) are included in our treatment of the lattice model below.

We notice that some of the values in Table IV, namely $J_x(S2, \overline{S3})$ and $J_y(S3, \overline{S3})$, are very small, which is expected to be a significant factor in the finite temperature behavior of our model. We demonstrate the domain wall that corresponds to $J_y(S3, \overline{S3})$ in Figure 11 via a top view. Because one of the $\dots\text{-Zr-O-Zr-O}\dots$ chains along the y -direction in the $S3$ unit cell is approximately aligned with the valley between consecutive Si dimers along the x -direction, it is approximately unchanged under the $S3 \rightarrow \overline{S3}$ transformation. Therefore when $S3$ and $\overline{S3}$ cells are attached in the y -direction, continuous and linear $\dots\text{-Zr-O-Zr-O}\dots$ chains are obtained (the top and bottom black horizontal straight lines in Figure 11). The remaining $\dots\text{-Zr-O-Zr-O}\dots$ chain in the unit cells matches imperfectly, but the distortion is small (the winding black horizontal curve in the middle in Figure 11) such that the only atom with a slightly modified

Domain boundary	J_x (eV)	J_y (eV)
$S1, \overline{S1}$	0.26	1.35
$S1, S2$	0.76	1.13
$S1, \overline{S2}$	0.96	0.99
$S1, S3$	0.61	4.81
$S1, \overline{S3}$	0.44	1.75
$S2, \overline{S2}$	0.38	1.64
$S2, S3$	0.17	0.98
$S2, \overline{S3}$	0.01	0.91
$S3, \overline{S3}$	0.73	0.002

Table IV. Domain boundary energies between low-energy states as computed from first principles. These energies, along with the couplings that include the states $S4$, $\overline{S4}$, $S5$ and $\overline{S5}$ reported in Table 1 of the Supplementary Material, serve as the couplings of nearest neighbors in our lattice model.

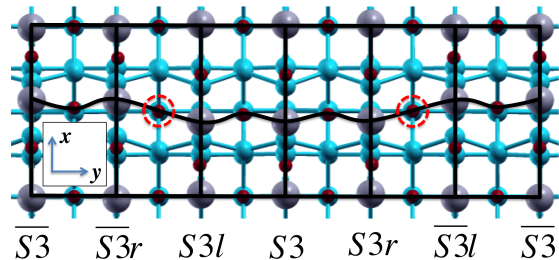


Figure 11. Top view of the domain boundaries along the x -direction between $S3$ and $\overline{S3}$, computed by stacking 3 unit cells of each structure along the y -direction. The domain energy, computed to be $J_y(S3, \overline{S3}) = 0.002$ eV per unit length, is very small due to the near-perfect meshing of the $\dots\text{-Zr-O-Zr-O}\dots$ chains in this configuration.

environment is one of the oxygen atoms at the domain boundary (encircled with a red dashed ring in the figure). This near-perfect meshing of the $\dots\text{-Zr-O-Zr-O}\dots$ chains after stacking the $S3$ and $\overline{S3}$ structures along the y -direction is the cause of the very small energy cost of creating the domain boundary.

The model we have built is a general discrete lattice model that resembles two dimensional Ising models and, more generally, Potts models [24]. However, due to the lack of any simple pattern in site energies and couplings, it does not belong to any analytically solvable category of models.

3. Mean-field approach

To understand the thermodynamic behavior of this model at finite temperature, we begin with the standard mean-field approach which is based on the assumption that every site interacts in an averaged manner with its neighboring sites. For a model with N states $\sigma_1, \sigma_2, \dots, \sigma_N$, every site has a probability $p(\sigma_i)$ of being occupied by state σ_i . In mean field theory, the energy of such a site including its interactions with its nearest neighbors is given by

$$U(\sigma_i) = E(\sigma_i) + 2 \sum_{j=1}^N p(\sigma_j) J_x(\sigma_i, \sigma_j) + 2 \sum_{j=1}^N p(\sigma_j) J_y(\sigma_i, \sigma_j). \quad (2)$$

The probability $p(\sigma_i)$ is given by the Boltzmann factor so that

$$p(\sigma_i) = \frac{\exp\left(-\frac{U(\sigma_i)}{k_B T}\right)}{Z}, \quad (3)$$

where

$$Z = \sum_{j=1}^N \exp\left(-\frac{U(\sigma_j)}{k_B T}\right) \quad (4)$$

is the mean-field partition function.

These equations form a self-consistent system of N equations for $p(\sigma_i)$ for a given temperature T and the specified energies $E(\sigma_i)$ and couplings J_x, J_y . We present the solutions of this system of equations for temperatures ranging from 0.1 through 3.0 eV/k_B in Figure 12. We find that there is a first-order phase transition at a very high temperature of $k_B T = 1.4$ eV ($\sim 16,000$ K). Below this temperature, one of the two degenerate ground states ($S1$ or $\bar{S1}$) occupies nearly all the sites (i.e., spontaneous symmetry breaking). Above the transition temperature, the ground states are suppressed and the lattice gets filled by the remaining states with an approximately equal contributions. At very high temperature (not shown in the figure), all states have equal probability, as expected.

It is known that in simpler two dimensional lattice problems, the mean-field approximation predicts correctly the existence of a phase transition but overestimates the critical temperature [25]. The mean-field approach assumes that each site interacts with all its neighbors in an uncorrelated fashion and neglects the fact that correlation lengths are finite. Moreover, as seen from equation (2), the mean-field equations sum over all neighbors and end up providing ‘‘isotropic solutions’’ (i.e., the x and y directions become equivalent), which is a serious shortcoming due to the major role anisotropy is expected to, and will, play in our system (see IV). In summary, we expect these mean field theory predictions to be informative but not quantitatively accurate.

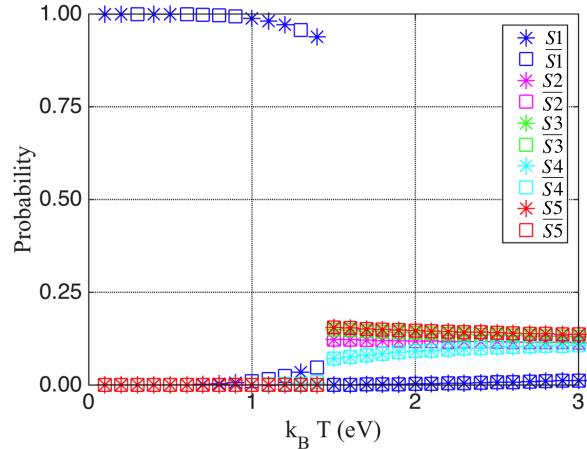


Figure 12. Probabilities of finding a type of state at an arbitrary site vs temperature, as computed by the mean-field equations for our lattice model.

4. Monte Carlo simulations

For a better understanding of our model at temperatures of practical interest, we have employed classical Monte Carlo simulations with a modified version of the Wolff cluster algorithm [26, 27] that we have developed. For further details of the method, we refer the reader to the Supplementary Material. We have run simulations in a 50×150 lattice with free boundary conditions (i.e., the lattice is a finite-sized system with zero couplings beyond the edges; comparison to periodic boundary conditions showed no discernible differences for this lattice size at the temperatures examined below). and completely random initial conditions, for $k_B T = 0.016, 0.032, 0.064, 0.128, 0.256$ and 0.512 eV. We have used a non-square simulation lattice because of the larger couplings in the y -direction compared to the x -direction, which lead to longer correlation lengths in the y -direction (see below). In Figure 13, a sample configuration of a well-thermalized simulation with $k_B T = 0.016$ eV ($T = 186$ K) is displayed.

In Figure 14, the autocorrelation functions $C_{\text{auto}}^{(k)}(t)$ as a function of simulation step (‘‘time’’ t) and the horizontal and vertical spatial correlation functions $C_x^{(k)}(\Delta i)$ and $C_y^{(k)}(\Delta j)$ are plotted for each state k for one particular Monte Carlo run. These correlation functions are defined as

$$C_{\text{auto}}^{(k)}(\Delta t) = \text{mean}_{i,j,t} [\langle \sigma_k(i, j, t) \sigma_k(i, j, t + \Delta t) \rangle - \langle \sigma_k(i, j, t) \rangle \langle \sigma_k(i, j, t + \Delta t) \rangle], \quad (5)$$

$$C_x^{(k)}(\Delta i) = \text{mean}_{i,j,t} [\langle \sigma_k(i, j, t) \sigma_k(i + \Delta i, j, t) \rangle - \langle \sigma_k(i, j, t) \rangle \langle \sigma_k(i + \Delta i, j, t) \rangle], \quad (6)$$

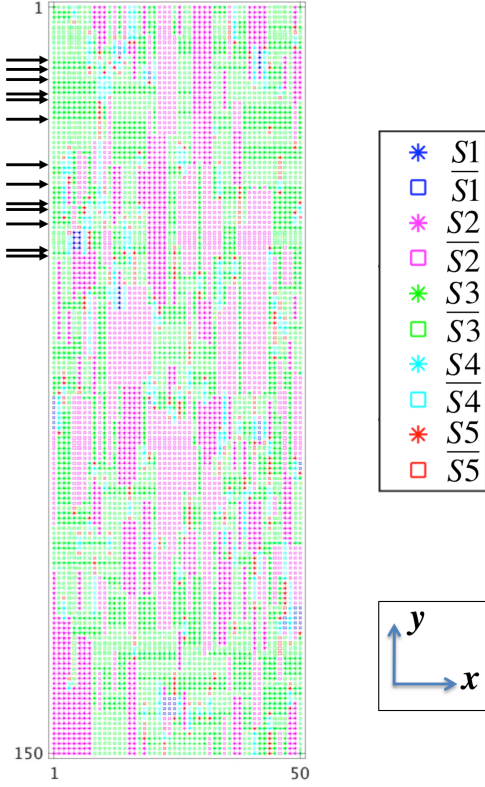


Figure 13. A snapshot of the Monte Carlo simulation of the lattice model at $k_B T = 0.016$ eV ($T = 186$ K). On the left edge of the simulation frame, a series of domain walls along the x -direction between $S3$ and $\overline{S3}$ domains are emphasized by black arrows.

$$C_y^{(k)}(\Delta j) = \text{mean}_{i,j,t} [\langle \sigma_k(i,j,t) \sigma_k(i,j + \Delta j, t) \rangle - \langle \sigma_k(i,j,t) \rangle \langle \sigma_k(i,j + \Delta j, t) \rangle], \quad (7)$$

where $\sigma_k(i,j,t)$ identifies the state at the lattice site (i,j) at the simulation time step t . We have defined 10 functions $\sigma_k(i,j,t)$ (one for each state k) such that $\sigma_k(i,j,t) = 1$ if the lattice site (i,j) is occupied by state k at time t and is 0 otherwise. In Figure 13, correlation functions for every type of state ($S1$, $\overline{S1}$ etc.) are computed separately and overlaid.

We observe that for the run exemplified by Figure 13 and analyzed in Figure 13, (1) a 1000 step Monte Carlo simulation leads to decorrelation (i.e., equilibration) of states $S1$, $\overline{S1}$, $S4$, $\overline{S4}$, $S5$ and $\overline{S5}$ but not for $S2$, $\overline{S2}$, $S3$ and $\overline{S3}$. (2) The simulation cell of size 50×150 is successful in containing the domains that form at this temperature since the spatial correlations become quite small by the half-way point along each direction of the simulation cell: sites that are sufficiently far from each other are not correlated. We have repeated these simulations 10 times for each temperature and have found that the correlation functions behave similarly when the ini-

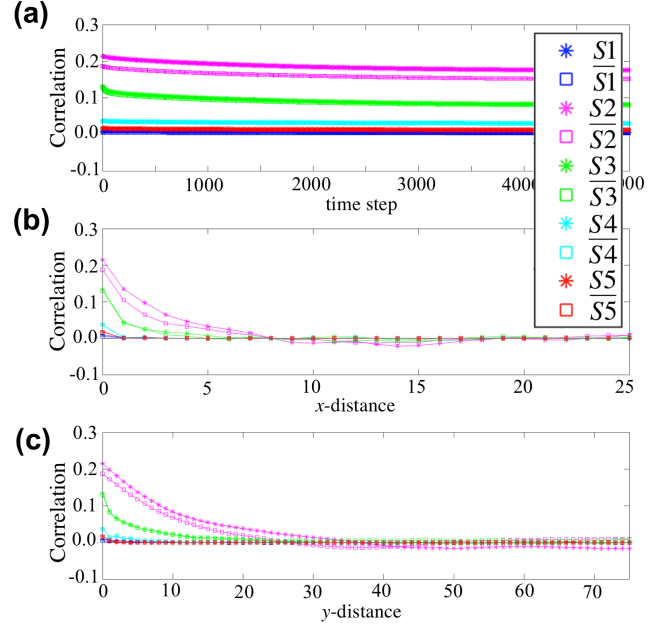


Figure 14. Temporal and spatial correlation functions for all 10 states for a Monte Carlo simulation with $k_B T = 0.016$ eV. (a) Temporal correlation (autocorrelation) functions as defined by equation (5), (b) correlation functions along the x -direction as per equation (6), and (c) correlation functions along the y -direction as per equation (7).

tial state of the simulation cell is chosen randomly. For temperatures higher than 0.128 eV, all temporal correlations decay below 0.1 in the duration of the simulation.

The reason behind the slow temporal decay of the $S2$, $\overline{S2}$, $S3$ and $\overline{S3}$ autocorrelations at low temperatures is that large domains of these states form in the lattice, and the Monte Carlo algorithm becomes inefficient in “flipping” these domains to another configuration. To see what other effects are present in these simulations, we monitor two other quantities displayed in Figure 15. The first is the probability that any lattice site is occupied by a particular state: we show the ratio of the number of sites occupied by a particular state to the total number of sites in the simulation cell. The second quantity is the average domain size for each state: this is computed for each snapshot at a fixed time by first determining all the domains of that state (including domains with only one site), and then dividing the total number of sites occupied by the state to the number of domains. A large jump in the second quantity during the simulation usually indicates a merger of two domains. The fact that these quantities change quickly at the beginning of the simulation and more slowly toward the end of the simulation in Figure 15 is indicative that the characteristics seen in Figure 13 are representative of large volumes of the configuration space sampled with the Boltzmann dis-

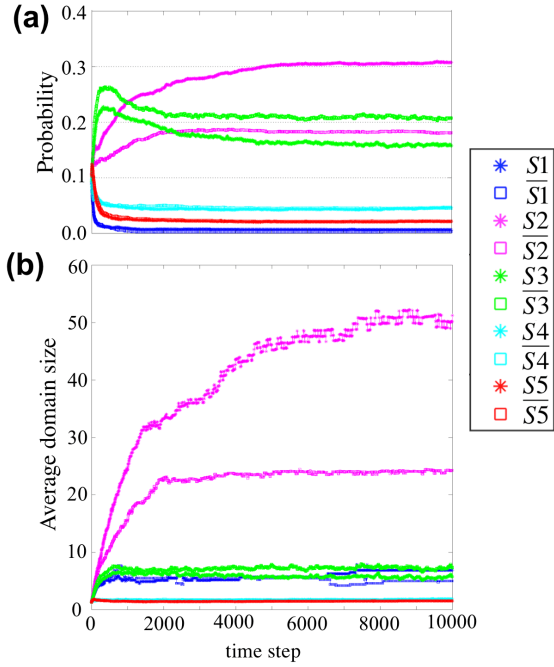


Figure 15. Probabilities of finding a state at an arbitrary site (a) and average domain sizes of each state (b), as they evolve during a Monte Carlo simulation for $k_B T = 0.016$ eV.

tribution at $k_B T = 0.016$ eV (186 K): namely, while the lattice system has not fully equilibrated, i.e., the temporal correlations have not decayed to very small values, it is not very far from equilibrium either. Hence, these results show that at this low temperature, the lattice system should be dominated by large domains of $S2$ and $\overline{S2}$ followed by smaller domains of $S3$ and $\overline{S3}$.

We now return to the mean field prediction that at temperatures lower than 1.4 eV the system should be dominated by either one of the ground states. Clearly, this prediction is not supported by our Monte Carlo simulations. Our Monte Carlo simulations show that for $k_B T \gtrsim 0.5$ eV, there is no long range order. In 16, we plot the correlation lengths ξ_x and ξ_y along the x - and y -directions, respectively. The correlation lengths are calculated by fitting the spatial correlation functions $C_x^{(k)}(\Delta x)$ and $C_y^{(k)}(\Delta y)$ to exponentials of the form $A \exp(-\Delta\alpha/\xi_\alpha)$. We calculate the correlation lengths (averaged over all states) for each run and then average over all runs at a given temperature. As indicated by the temperature dependence of the correlation length ξ_y , the system gradually becomes more ordered as the temperature is increased up to 0.128 eV, and then becomes disordered. Such behavior is associated with a second order phase transition in which correlation lengths diverge upon approaching the critical temperature. If such a critical temperature is present in this system, it lies

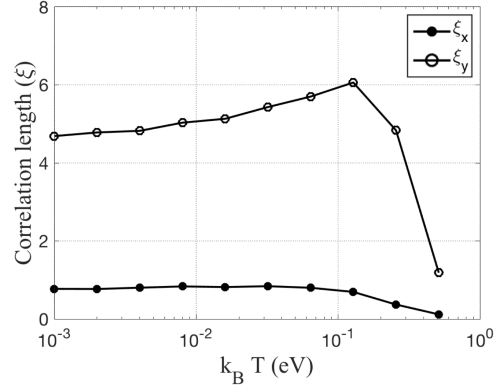


Figure 16. Correlation lengths along the x - and y -directions vs temperature. Each data point is obtained by fitting an exponential decay function to spatial correlation functions for each run at a given temperature, and then averaging the results of the fit for all the runs at that temperature.

between 0.128 eV (~ 1500 K) and 0.256 eV (~ 3000 K). Because the melting temperature of silicon is ~ 1700 K, it is likely impossible to approach this critical temperature in practice. Hence, it is safe to assume that for the relevant experimental conditions ($T < 1000$ K), the monolayer system is well within the ordered phase.

Finally, we comment on qualitative characteristics of the multi-domain structure of these films based on our lattice model. In Figure 17, we display the probability for a site to be occupied by each state as a function of temperature, where the probability values are averaged over the last quarter of each run, and then further averaged over 10 runs. The data show that the system is dominated by the second and the third lowest energy configurations ($S2, S3, \overline{S2}, \overline{S3}$). As discussed above, we believe that this is due to the rather low couplings $J_x(S2, \overline{S3})$ and $J_y(S3, \overline{S3})$ when compared to the other couplings in Table IV. Namely, these domain walls are not very costly energetically, so their entropic contribution is significant even at low temperatures and stabilizes these phases even though they are not the lowest energy states.

In Figure 18 we display the average domain size of each state vs temperature, again averaged over 10 runs for each temperature. We find that, on average, the domains of states $S2$ and $\overline{S2}$ are larger than the domains of states $S3$ and $\overline{S3}$, even though they occupy similar portions of the simulation cell (see 17). This may be because $J_y(S3, \overline{S3}) = 0.002$ eV so the $S3$ and $\overline{S3}$ easily form vertical stacks of domains at essentially no energetic cost, as exemplified in Figure 13: some of these stacks are emphasized by black arrows on the left edge of the figure, but there are many more in the interior of the simulation cell.

being due to a transition between these two states.

IV. CONCLUSION

We have conducted a computational study of ZrO_2 monolayers on Si(001) using DFT. These monolayers have recently been grown with as an abrupt oxide/semiconductor interface but with an amorphous structure and are measured to be ferroelectric [1]. In our computations, we have found a multiplicity of (meta)stable structures with a large variation in ionic polarization but small differences in energy, atomic structure and chemistry. This suggests that achieving epitaxy in the experiment should be challenging. In order to understand the finite-temperature behavior of these ultrathin films, we have developed a two dimensional discrete lattice model of the domains in these thin films using DFT-derived parameters. We have employed mean-field and Monte Carlo calculations to study this lattice model and concluded that two distinct and oppositely polarized structures, namely $S2$, $S3$ and their counterparts $\overline{S2}$ and $\overline{S3}$, dominate the films at the temperatures of interest. The ferroelectric switching observed in the experiment is explained by the film locally adopting one of these two structures and locally switching between them. We have found that for monocrystalline epitaxial films, this switching leads to a VBE shift in silicon of $\Delta V = 0.6$ eV, which is moderately greater than the experimental value of $\Delta V = 0.4$ eV, in agreement with the idea of partial (local) polarization switching.

V. ACKNOWLEDGEMENTS

This work was supported primarily by the grant NSF MRSEC DMR-1119826. We thank the Yale Center for Research Computing for guidance and use of the research computing infrastructure, with special thanks to Stephen Weston and Andrew Sherman. Additional computational support was provided by NSF XSEDE resources via Grant TG-MCA08X007.

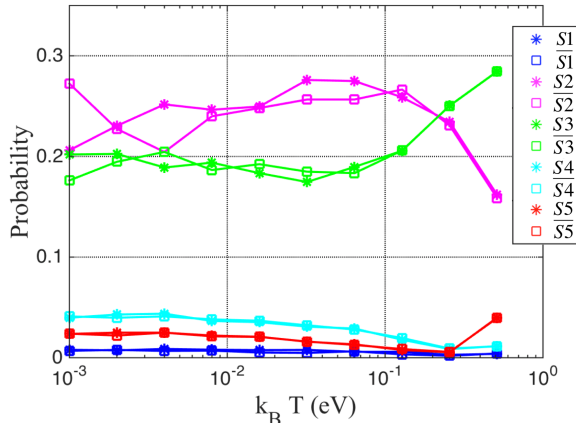


Figure 17. Probabilities of finding a state at an arbitrary site vs temperature, as computed by Monte Carlo simulations. For each temperature, the probabilities are averaged over the last quarter of each run, and then further averaged over 10 runs.

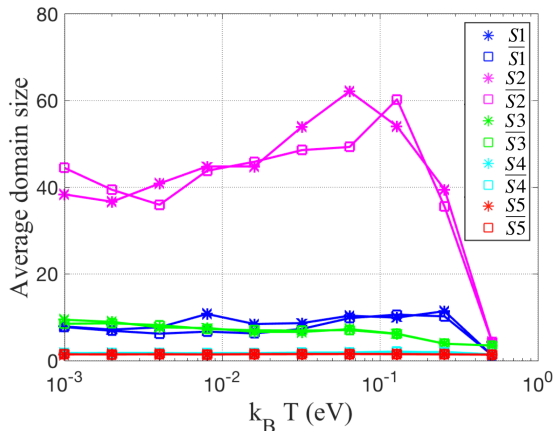


Figure 18. Average domain size for each type of state vs temperature, as computed by Monte Carlo simulations. For each temperature, the domain sizes are averaged over the last quarter of each run, and then further averaged over 10 runs.

To sum up, according to our discrete lattice model simulations, for 2×1 ordered ZrO_2 monolayers on the Si(001) surface and the experimentally relevant temperature range of 200 – 1000 K, domains of $S2$, $\overline{S2}$, $S3$ and $\overline{S3}$ should be expected to occur with linear extents ranging from a few to a few dozen unit cells. This supports our claim that achieving epitaxy for these films should be challenging. However, given that the local structure is approximated by a mixture of $S2$ and $S3$ domains, the observed ferroelectric switching is understandable as

- [1] M. Dogan, S. Fernandez-Peña, L. Kornblum, Y. Jia, D. P. Kumah, J. W. Reiner, Z. Krivokapic, A. M. Kolpak, S. Ismail-Beigi, C. H. Ahn, et al., *Nano Letters* **18**, 241 (2018), ISSN 1530-6984, URL <http://dx.doi.org/10.1021/acs.nanolett.7b03988>.
- [2] H. Y. Hwang, Y. Iwasa, M. Kawasaki, B. Keimer, N. Nagao, and Y. Tokura, *Nature Materials* **11**, 103 (2012), ISSN 1476-1122, URL <http://www.nature.com/nmat/journal/v11/n2/abs/nmat3223.html>.
- [3] J. Mannhart and D. G. Schlom, *Science* **327**, 1607 (2010), ISSN 0036-8075, 1095-9203, URL <http://science.sciencemag.org/content/327/5973/1607>.

- [4] J. W. Reiner, F. J. Walker, and C. H. Ahn, *Science* **323**, 1018 (2009), ISSN 0036-8075, 1095-9203, URL <http://www.sciencemag.org/content/323/5917/1018>.
- [5] J. W. Reiner, A. M. Kolpak, Y. Segal, K. F. Garrity, S. Ismail-Beigi, C. H. Ahn, and F. J. Walker, *Advanced Materials* **22**, 2919 (2010), ISSN 1521-4095, URL <http://onlinelibrary.wiley.com/doi/10.1002/adma.200904306/abstract>.
- [6] M. Dogan and S. Ismail-Beigi, *Physical Review B* **96**, 075301 (2017), URL <https://link.aps.org/doi/10.1103/PhysRevB.96.075301>.
- [7] R. A. McKee, F. J. Walker, and M. F. Chisholm, *Science* **293**, 468 (2001), ISSN 0036-8075, 1095-9203, URL <http://www.sciencemag.org/content/293/5529/468>.
- [8] K. F. Garrity, A. M. Kolpak, and S. Ismail-Beigi, *Journal of Materials Science* **47**, 7417 (2012), ISSN 0022-2461, 1573-4803, URL <http://link.springer.com/article/10.1007/s10853-012-6425-z>.
- [9] I. P. Batra, P. Wurfel, and B. D. Silverman, *Physical Review B* **8**, 3257 (1973), URL <http://link.aps.org/doi/10.1103/PhysRevB.8.3257>.
- [10] C. Dubourdieu, J. Bruley, T. M. Arruda, A. Posadas, J. Jordan-Sweet, M. M. Frank, E. Cartier, D. J. Frank, S. V. Kalinin, A. A. Demkov, et al., *Nature Nanotechnology* **8**, 748 (2013), ISSN 1748-3387, URL <http://www.nature.com/nnano/journal/v8/n10/full/nnano.2013.192.html>.
- [11] J. Robertson, *Reports on Progress in Physics* **69**, 327 (2006), ISSN 0034-4885, URL <http://iopscience.iop.org/0034-4885/69/2/R02>.
- [12] M. D. McDaniel, T. Q. Ngo, A. Posadas, C. Hu, S. Lu, D. J. Smith, E. T. Yu, A. A. Demkov, and J. G. Ekerdt, *Advanced Materials Interfaces* **1**, n/a (2014), ISSN 2196-7350, URL <http://onlinelibrary.wiley.com/doi/10.1002/admi.201400081/abstract>.
- [13] R. A. McKee, F. J. Walker, and M. F. Chisholm, *Physical Review Letters* **81**, 3014 (1998), URL <http://link.aps.org/doi/10.1103/PhysRevLett.81.3014>.
- [14] D. P. Kumah, M. Dogan, J. H. Ngai, D. Qiu, Z. Zhang, D. Su, E. D. Specht, S. Ismail-Beigi, C. H. Ahn, and F. J. Walker, *Physical Review Letters* **116**, 106101 (2016), URL <http://link.aps.org/doi/10.1103/PhysRevLett.116.106101>.
- [15] J. P. Perdew, K. Burke, and M. Ernzerhof, *Physical Review Letters* **77**, 3865 (1996), URL <http://link.aps.org/doi/10.1103/PhysRevLett.77.3865>.
- [16] D. Vanderbilt, *Physical Review B* **41**, 7892 (1990), URL <http://link.aps.org/doi/10.1103/PhysRevB.41.7892>.
- [17] P. Giannozzi, S. Baroni, N. Bonini, M. Calandra, R. Car, C. Cavazzoni, Davide Ceresoli, G. L. Chiarotti, M. Cococcioni, I. Dabo, et al., *Journal of Physics: Condensed Matter* **21**, 395502 (2009), ISSN 0953-8984, URL <http://stacks.iop.org/0953-8984/21/i=39/a=395502>.
- [18] N. Marzari, D. Vanderbilt, A. De Vita, and M. C. Payne, *Physical Review Letters* **82**, 3296 (1999), URL <http://link.aps.org/doi/10.1103/PhysRevLett.82.3296>.
- [19] L. Bengtsson, *Physical Review B* **59**, 12301 (1999), URL <http://link.aps.org/doi/10.1103/PhysRevB.59.12301>.
- [20] G. Henkelman, B. P. Uberuaga, and H. Jónsson, *The Journal of Chemical Physics* **113**, 9901 (2000), ISSN 0021-9606, 1089-7690, URL <http://scitation.aip.org/content/aip/journal/jcp/113/22/10.1063/1.1329672>.
- [21] A. Ramstad, G. Brocks, and P. J. Kelly, *Physical Review B* **51**, 14504 (1995), URL <http://link.aps.org/doi/10.1103/PhysRevB.51.14504>.
- [22] Ó. Paz, A. J. R. da Silva, J. José Sáenz, and E. Artacho, *Surface Science* **482–485**, Part 1, 458 (2001), ISSN 0039-6028, URL <http://www.sciencedirect.com/science/article/pii/S0039602800010220>.
- [23] A. V. Bune, V. M. Fridkin, S. Ducharme, L. M. Blinov, S. P. Palto, A. V. Sorokin, S. G. Yudin, and A. Zlatkin, *Nature* **391**, 874 (1998), ISSN 0028-0836, URL <http://www.nature.com/nature/journal/v391/n6670/full/391874a0.html>.
- [24] F. Y. Wu, *Reviews of Modern Physics* **54**, 235 (1982), URL <http://link.aps.org/doi/10.1103/RevModPhys.54.235>.
- [25] M. A. Neto, R. A. dos Anjos, and J. R. de Sousa, *Physical Review B* **73**, 214439 (2006), URL <http://link.aps.org/doi/10.1103/PhysRevB.73.214439>.
- [26] R. H. Swendsen and J.-S. Wang, *Physical Review Letters* **58**, 86 (1987), URL <http://link.aps.org/doi/10.1103/PhysRevLett.58.86>.
- [27] U. Wolff, *Physical Review Letters* **62**, 361 (1989), URL <http://link.aps.org/doi/10.1103/PhysRevLett.62.361>.

Supplementary Material for “Theory of Ferroelectric ZrO₂ Monolayers on Si”

Mehmet Dogan^{1,2,3,4} and Sohrab Ismail-Beigi^{1,2,5,6}

¹Center for Research on Interface Structures and Phenomena, Yale University, New Haven, Connecticut
06520, USA

²Department of Physics, Yale University, New Haven, Connecticut 06520, USA

³Department of Physics, University of California, Berkeley, 94720 USA

⁴Materials Science Division, Lawrence Berkeley National Laboratory, Berkeley, California 94720, USA

⁵Department of Applied Physics, Yale University, New Haven, Connecticut 06520, USA

⁶Department of Mechanical Engineering and Materials Science, Yale University, New Haven, Connecticut
06520, USA

Monte Carlo algorithms for statistical physics

A thermodynamic system is described by its partition function

$$Z = \sum_{\{s\}} e^{-\frac{E_s}{k_B T}}, \quad (1)$$

where the sum runs over all possible states of the system, E_s is the energy of state s , k_B is Boltzmann’s constant and T is the temperature. The expectation value of an observable X is

$$\langle X \rangle = \frac{1}{Z} \sum_{\{s\}} X_s e^{-\frac{E_s}{k_B T}}, \quad (2)$$

where X_s is the value of the observable X when the system is in state s .

The summations are over all possible states of the system which is a space that is enormous for most physically relevant systems. However, most of the states occur with vanishingly small probabilities, computed by the formula $\frac{1}{Z} \exp\left(-\frac{E_s}{k_B T}\right)$. Hence in order to avoid summing over all possible states, which is an intractable problem and a wasteful attempt, one usually uses *importance sampling*, in which the sampling is done over states that are chosen according to the probability distribution $\frac{1}{Z} \exp\left(-\frac{E_s}{k_B T}\right)$ [1].

Given two states of the system and their energies, it is trivial to compute their relative probabilities according to their Boltzmann factors $\exp\left(-\frac{E_s}{k_B T}\right)$. However, computing the absolute probability of a state requires computing Z , which we wish to avoid. The most commonly used way of computing expectation values without evaluating the partition function is by creating a Markov chain of states in which each state only depends on the state that immediately precedes it [2]. Starting from a configuration S_i with a Boltzmann factor p_i , a new trial configuration S_j with a Boltzmann factor p_j is generated and accepted with probability π_{ij} . The probability of occupying the state S_j should be equal to the sum of the probabilities of arriving at state S_j from any given state S_i , i.e.

$$\sum_i p_i \pi_{ij} = p_j. \quad (3)$$

At equilibrium, this Markov process should obey *detailed balance*, i.e.

$$p_i \pi_{ij} = p_j \pi_{ji}. \quad (4)$$

In general, the transition probabilities π_{ij} are the product of two factors: a probability g_{ij} of proposing to move to state S_j from state S_i , and an acceptance ratio A_{ij} of accepting the proposed transition from S_i to S_j . Thus we can write

$$p_i g_{ij} A_{ij} = p_j g_{ji} A_{ji}, \quad (5)$$

or

$$\frac{g_{ij} A_{ij}}{g_{ji} A_{ji}} = \exp\left(-\frac{E_j - E_i}{k_B T}\right). \quad (6)$$

For a given problem, g_{ij} , A_{ij} are specified by the algorithm such that Equation (6) is satisfied and the sampling efficiency is maximized.

Finally, a valid Monte Carlo algorithm must be ergodic, i.e., any state must be reachable from any other state via a succession of moves.

Metropolis algorithms for discrete lattice models

The most common Monte Carlo algorithm for discrete lattice models such as the Ising model is the so-called Metropolis algorithm. Let us describe this algorithm in the context of our lattice model which we describe in more detail in the main text.

The Hamiltonian of our two dimensional discrete lattice model is

$$H = \sum_{i,j} E(\sigma(i,j)) + \sum_{i,j} J_x(\sigma(i,j), \sigma(i+1,j)) + \sum_{i,j} J_y(\sigma(i,j), \sigma(i,j+1)), \quad (7)$$

where (i, j) are the positions on the discrete lattice along the (x, y) -directions, $\sigma(i, j)$ is the state on lattice site (i, j) , $E(\sigma(i, j))$ is the site energy of the state $\sigma(i, j)$, $J_x(\sigma(i, j), \sigma(i+1, j))$ is the nearest-neighbor interaction energy along the x -direction, and $J_y(\sigma(i, j), \sigma(i, j+1))$ is the nearest-neighbor interaction energy along the y -direction. $J_x(\sigma_1, \sigma_2) = J_y(\sigma_1, \sigma_2) = 0$ if $\sigma_1 = \sigma_2$. In this model, there are N types of states, i.e. σ is a function that maps a lattice site onto one of s_1, s_2, \dots, s_N . Note that the lower-case s are different from the upper-case S used above, which denoted the state of the whole system, which would be the collection of states s on all lattice points for this model.

The two dimensional Ising model is a special case of our model, where $N = 2$. The external magnetic field can be included by having $E(s_1) \neq E(s_2)$, and anisotropy can be included by having $J_x(s_1, s_2) \neq J_y(s_1, s_2)$.

The Metropolis algorithm would operate on our N -state model as follows:

1. Pick a lattice site at random. Let us call the state on the site s_i . Let us call the state of the initial system S_μ .
2. Propose to flip the state s_i to another state s_f , chosen among all non- s_i states with equal probability $\frac{1}{N-1}$. Let us call the state of the system if the proposed flip occurs S_ν . Thus $g_{\mu\nu} = \frac{1}{N-1}$ (see Equation (6)). The probability of proposing the inverse move, i.e. going to S_μ from S_ν is clearly the same, hence $g_{\nu\mu} = g_{\mu\nu} = \frac{1}{N-1}$.
3. Compute the energy difference $E_\nu - E_\mu$ between S_ν and S_μ . This is simple, since the only difference is the state change of state s_i to s_j , and the energy difference is localized to the site energy and the couplings with the nearest neighbors of that site.

4. The acceptance ratios are obtained by Equation (6):

$$\frac{A_{\mu\nu}}{A_{\nu\mu}} = \exp\left(-\frac{E_\nu - E_\mu}{k_B T}\right). \quad (8)$$

A common way of achieving this equation is by setting:

$$A_{\mu\nu} = \begin{cases} \exp\left(-\frac{E_\nu - E_\mu}{k_B T}\right) & \text{if } E_\nu > E_\mu \\ 1 & \text{if } E_\nu \leq E_\mu \end{cases} \quad (9)$$

To find the expectation value of an observable X , X is computed at each step of the simulation that comprises of a finite number of steps, and then simply averaged. This is the merit of *importance sampling*, which takes care of the relative probabilities of states through Equation (6), therefore the observables can simply be averaged.

Wolff cluster algorithms

The success of a Monte Carlo algorithm is usually measured by how easy it can generate “independent” samples, i.e. how many attempts it takes to go from a state S_μ to another state S_ν such that S_μ and S_ν are “uncorrelated” (namely, decorrelation time). The “single-flip” Metropolis algorithm is conceptually simple and easy to implement. However, at each simulation step, the state only slightly changes, so the decorrelation time can be large. For models with a second order phase transition, such as the two dimensional Ising model, this algorithm suffers from “critical slowing down” where, close to the critical temperature of the model, the decorrelation time diverges [3].

This issue can be solved by algorithms that propose states that are sufficiently modified from the preceding state. A family of such algorithms is called cluster algorithms, where rather than switching the state on a single site, the state on a groups of sites (“a cluster”) is switched simultaneously [4]. Here we modify the Wolff cluster algorithm [5], originally developed for the Ising model, to simulate our N -state model:

1. Pick a lattice site i at random. Let us call the state on the site s_i . Let us call the state of the initial system S_μ .
2. Add each of the nearest neighbors j of the site i to the cluster, with the probability p_{add} , provided

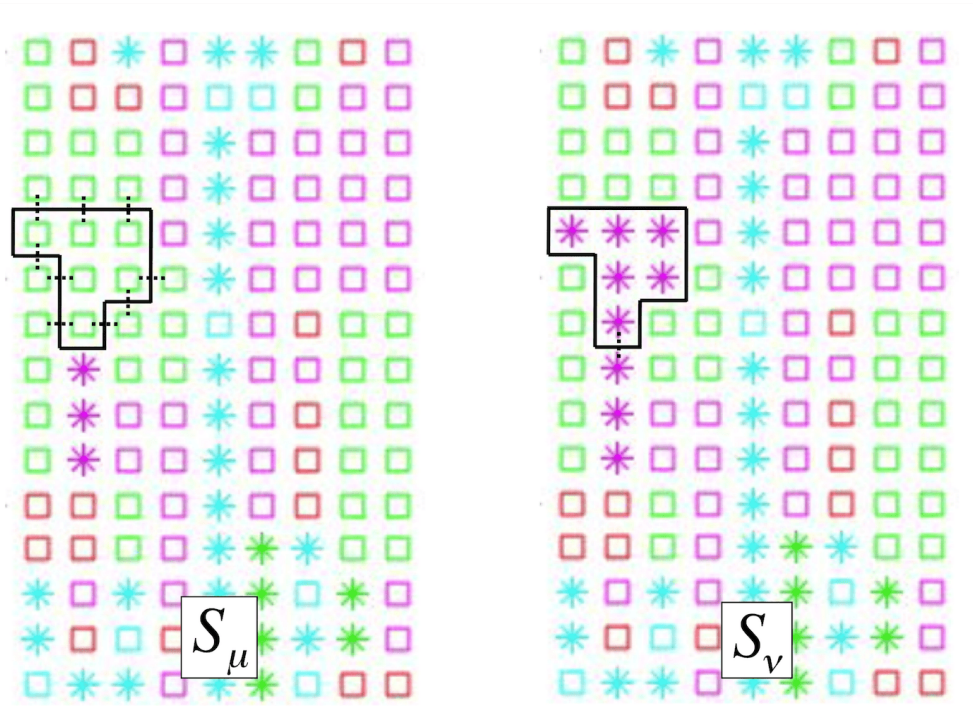


Figure 1: A sample instant of a Wolff cluster simulation of an N -state lattice model, prior to (S_μ) and after (S_ν) the switching of a cluster. The boundary of the cluster is shown by solid lines, and the bonds at the boundary of the cluster are shown by dotted lines. Each color-shape combination denotes a type of state in our 10-state lattice model, described in detail in the main text.

that the states on sites i and j are the same, and the “bond” between i and j has not yet been considered.

3. Once all the neighbors of site i have been considered, move to the next site in the cluster. Repeat step 2 for this site. If all the sites in the cluster have gone through step 2, the cluster has been built. Move to step 4.
4. Propose to flip the state s_i to another state s_f , chosen among all non- s_i states with equal probability $\frac{1}{N-1}$, for all the sites in the cluster. Let us call the state of the system if the proposed flip occurs S_ν .
5. Compute the number of bonds at the boundary of the cluster. The two neighboring states of the same kind are said to have a bond that is intact. When the cluster is “flipped” the bonds at the boundary will be broken. In Figure 1, we illustrate the formation of a cluster for a given state S_μ of the lattice, shown on the left. The number of bonds at the boundary (shown as dotted lines in the figure) is $n_\mu = 9$. The proposed state S_ν is shown on the right. The number of bonds at the boundary in the proposed state is $n_\nu = 1$.

6. Compute the energy difference $E_\nu - E_\mu$ between S_ν and S_μ . This requires accounting for all the nearest-neighbor interactions at the boundary of the cluster in both the initial and the final states.

Finding the correct acceptance ratio for this algorithm is somewhat involved. Let us assume that the cluster in S_μ in Figure 1 is built in the following order:

1. The site at the upper left corner of the cluster is randomly picked.
2. The site to the right is added with probability p_{add} , the other neighboring sites of the same kind (above and below) are rejected with probability $(1 - p_{\text{add}})^2$.
3. The site to the right is added with probability p_{add} , the other neighboring sites of the same kind (above and below) are rejected with probability $(1 - p_{\text{add}})^2$.
4. The site below is added with probability p_{add} , the site above is rejected with probability $(1 - p_{\text{add}})$.
5. The site to the left is added with probability p_{add} , the other neighboring sites of the same kind (to the right and below) are rejected with probability $(1 - p_{\text{add}})^2$.
6. The site below is added with probability p_{add} , the site to the left is rejected with probability $(1 - p_{\text{add}})$.
7. Both neighboring sites (to the left and to the right) are rejected with probability $(1 - p_{\text{add}})^2$.

The total probability of this process in this order is $p_{\text{add}}^5 (1 - p_{\text{add}})^{10}$. The same process can be repeated for the cluster in S_ν in Figure 1 built in the exact same order, which yields a probability of $p_{\text{add}}^5 (1 - p_{\text{add}})^2$.

The ratio of proposal probabilities of the forward and backward moves is then

$$\frac{p_{\text{add}}^5 (1 - p_{\text{add}})^{10}}{p_{\text{add}}^5 (1 - p_{\text{add}})^2} = (1 - p_{\text{add}})^8, \quad (10)$$

where 8 is the difference in the number of bonds at the boundary for S_μ and S_ν , i.e. $n_\mu - n_\nu = 8$. It is evident that for any given order for building the same cluster, the ratio of proposal probabilities of the forward and backward moves will be $(1 - p_{\text{add}})^{n_\mu - n_\nu}$. Because $g_{\mu\nu}$ is the sum of the probabilities of all moves that propose S_ν from S_μ and $g_{\nu\mu}$ is the sum of the probabilities of all moves that propose S_μ from S_ν , we can write

$$\frac{g_{\mu\nu}}{g_{\nu\mu}} = (1 - p_{\text{add}})^{n_\mu - n_\nu}. \quad (11)$$

Therefore Equation (6) yields

$$\begin{aligned} \frac{A_{\mu\nu}}{A_{\nu\mu}} &= (1 - p_{\text{add}})^{n_\nu - n_\mu} \exp\left(-\frac{E_\nu - E_\mu}{k_B T}\right) \\ &= \exp\left(-\frac{E_\nu - E_\mu - k_B T (n_\nu - n_\mu) \log(1 - p_{\text{add}})}{k_B T}\right). \end{aligned} \quad (12)$$

If we define

$$\Delta_{\mu\nu} \equiv E_\nu - E_\mu - k_B T (n_\nu - n_\mu) \log(1 - p_{\text{add}}), \quad (13)$$

we can set the acceptance ratios (in analogy with Equation (9)) to be

$$A_{\mu\nu} = \begin{cases} \exp\left(-\frac{\Delta_{\mu\nu}}{k_B T}\right) & \text{if } \Delta_{\mu\nu} > 0 \\ 1 & \text{if } \Delta_{\mu\nu} \leq 0 \end{cases}. \quad (14)$$

In the original Wolff cluster method for the Ising model, p_{add} is defined as a function of temperature such that the acceptance ratios are always 1. This makes for a rejection-less algorithm which is able to switch clusters of different sizes at any temperature. However, in our model there is no simple relationship between $E_\nu - E_\mu$ and $n_\nu - n_\mu$ as in there is in the Ising model. Therefore p_{add} cannot be defined *a priori* to make $\Delta_{\mu\nu}$ vanish in Equation (13), which in turn would guarantee $A_{\mu\nu} = 1$ in 14. After empirical tests on our simulations, we have set $p_{\text{add}} = \frac{1}{2}$ for the results presented in the main text. Improving the acceptance ratios through the choice of p_{add} is the subject of future research.

List of all domain wall energies

We tabulate all domain wall energies in table 1, which includes the couplings between $S1$, $S2$, $S3$ and their barred counterparts, also reported above in table ??.

A few of the couplings that involve the higher-energy $S4$ and $S5$ structures are negative, which can be understood in some cases when the domain boundary region resembles a lower energy structure. In figure 2, we illustrate the domain boundaries that correspond to $J_x(S3, S5) = -0.24$ eV. The structure immediately to the left of the right domain boundary ($S3r$) closely resembles the $S2$ structure (see Figure 5 in the main text). However, the fact that the higher energy $S4$ and $S5$ structures have negative domain wall energies with the lower energy structures in some cases is not enough to generate antiferroelectric patterns in our Monte Carlo simulations. This may be due to the separation of scale in the energies of

Domain boundary	J_x (eV)	J_y (eV)
$S1, \overline{S1}$	0.26	1.35
$S1, S2$	0.76	1.13
$S1, \overline{S2}$	0.96	0.99
$S1, S3$	0.61	4.81
$S1, \overline{S3}$	0.44	1.75
$S1, S4$	0.55	2.79
$S1, \overline{S4}$	-0.20	2.37
$S1, S5$	0.35	1.35
$S1, \overline{S5}$	0.40	0.56
$S2, \overline{S2}$	0.38	1.64
$S2, S3$	0.17	0.98
$S2, \overline{S3}$	0.01	0.91
$S2, S4$	-0.17	2.23
$S2, \overline{S4}$	0.86	2.28
$S2, S5$	0.34	0.59
$S2, \overline{S5}$	-0.12	1.31
$S3, \overline{S3}$	0.73	0.002
$S3, S4$	0.10	1.89
$S3, \overline{S4}$	0.23	1.84
$S3, S5$	-0.24	0.75
$S3, \overline{S5}$	0.69	1.21
$S4, \overline{S4}$	0.55	-0.33
$S4, S5$	0.71	0.65
$S4, \overline{S5}$	-0.26	1.86
$S5, \overline{S5}$	0.56	0.30

Table 1: Domain boundary energies computed from first principles. These energies serve as the couplings of nearest neighbors in our lattice model.

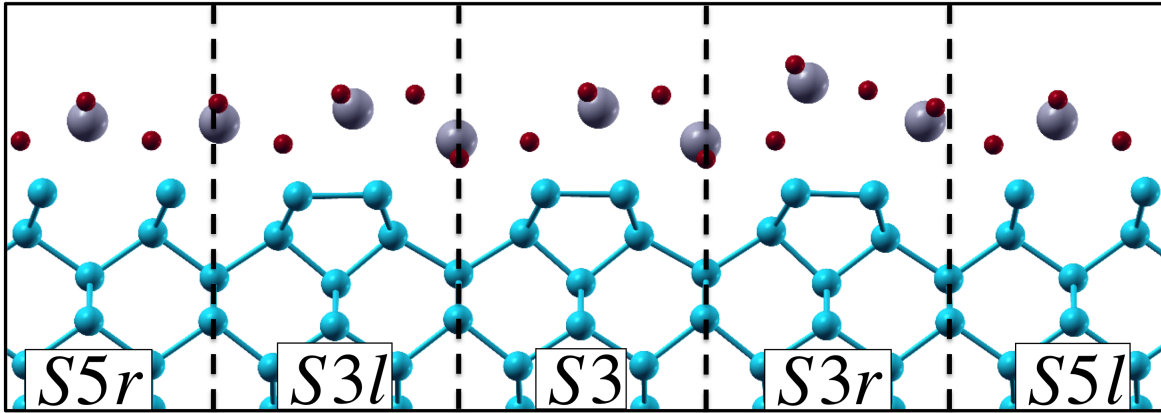


Figure 2: The domain boundaries along the y -direction between $S3$ and $S5$, computed by stacking 3 unit cells of each structure along the x -direction. The domain energy, computed to be $J_x(S5, S5) = -0.24$ eV per unit length, is negative partly due to the fact that the vicinity of one of the boundary walls (labelled $S3r$) resembles a lower energy configuration $S2$ (see Figure 5 in the main text).

the lowest three structures and $S4$ and $S5$ (see Table II in the main text). Hence the energy reduction achieved by making these domain boundaries (0.26 eV or less) is not enough to compensate for the high energy cost of creating these two structures in the first place.

Bibliography

- [1] E. Luijten, in *Computer Simulations in Condensed Matter Systems: From Materials to Chemical Biology Volume 1*, edited by M. F. Professor, G. C. Professor, and K. B. Professor (Springer Berlin Heidelberg, 2006), no. 703 in Lecture Notes in Physics, pp. 13–38, ISBN 978-3-540-35270-9 978-3-540-35273-0, DOI: 10.1007/3-540-35273-2_1, URL http://link.springer.com/chapter/10.1007/3-540-35273-2_1.
- [2] N. Metropolis, A. W. Rosenbluth, M. N. Rosenbluth, and A. H. Teller, *The Journal of Chemical Physics* **21**, 1087 (1953), ISSN 0021-9606, URL <http://aip.scitation.org/doi/abs/10.1063/1.1699114>.
- [3] G. T. Barkema and M. E. J. Newman, arXiv:cond-mat/9703179 (1997), arXiv: cond-mat/9703179, URL <http://arxiv.org/abs/cond-mat/9703179>.
- [4] R. H. Swendsen and J.-S. Wang, *Physical Review Letters* **58**, 86 (1987), URL <http://link.aps.org/doi/10.1103/PhysRevLett.58.86>.
- [5] U. Wolff, *Physical Review Letters* **62**, 361 (1989), URL <http://link.aps.org/doi/10.1103/PhysRevLett.62.361>.